

McNab, F., Sloan, R.A., and Walker, R.T., 2019, Simultaneous orthogonal shortening in the Afghan-Tajik Depression: Geology, <https://doi.org/10.1130/G46090.1>

EARTHQUAKE MODELING

Methods

We determined source parameters for four large earthquakes using the MT5 program of Zwick et al. (1994). MT5 uses an algorithm developed by McAffrey and Abers (1988) and McAffrey et al. (1991) to invert *P*- and *SH*-wave data for strike, dip, rake, scalar moment and source-time function. We follow procedures that are well established (e.g. Delouis et al., 2002; Bayasgalan et al., 2005; Emmerson et al., 2006; Sloan et al., 2011). The inversion uses only the long-period signal, reducing the sensitivity to small scale variations, allowing moderate-sized earthquakes to be treated as point sources. The source is constrained to be double-couple. Attenuation and geometrical spreading are corrected for using Futterman operators with $t^* = 1.0$ s and 4.0 s for *P*- and *SH*-waves, respectively. We weighted seismograms by azimuthal density and *SH*-wave data by half compared to *P*-wave data. We used the regional model of Kufner et al. (2018) to constrain the velocity structure around the source. This model includes a slow layer corresponding to the sedimentary cover of the Afghan-Tajik Depression. *P*-wave velocities were converted to *S*-wave velocity and density using the relationships of Brocher (2005).

For the 2014-11-14 event, data were too poor to perform an inversion for all source parameters. Instead, we constrained centroid depth as accurately as possible using the WKBJ3 program of Chapman (1978) and Chapman et al., (1998). Again, we follow procedures that are well established (e.g. Sloan et al., 2011). The program produces synthetic seismograms by

tracing rays through the Earth using the WKBJ approximation for turning waves and attenuation corresponding to $t^*=1.0$ s. The strike, dip and rake are fixed to the Global Centroid Moment Tensor (CMT) Catalog solution, and the AK135 global velocity model is used (Kennet et al., 1995). The program produces forward models, and depth is varied until a satisfactory visual fit to the real data is achieved.

Each of these methods aims to provide accurate estimates of centroid depth by modeling ‘depth phases’, i.e. rays which reflect off the Earth’s surface close to the earthquake epicenter. The phases pP , a P -wave reflection; sP , an S -wave converted to a P -wave on reflection; and sS , an S -wave reflection, are all included. Travel times of these depth phases relative to those of the direct phases is strongly dependent on the depth of the earthquake source.

Results

Results of earthquake modeling for each event are presented Figures DR1-DR5 and summarized in Table 1 of the main text. Data for the 1991-04-18, 1994-05-01, 2006-07-29a and 2006-07-29b events were inverted for all source parameters (Figures 1-4). Predicted seismograms generally provide an excellent fit to the data. Data for the 1991-04-18 are sparse and noisy, but an acceptable fit to the available data is achieved. In particular, seismogram widths (i.e. the separation of the direct and depth phases) are matched well, indicating that the estimated centroid depth is accurate. Data for the 2014-11-14 were too poor to perform an inversion for all source parameters. However, five seismograms were available in which the depth phases were clearly visible (examples are shown in Figure DR5). Synthetic seismograms computed for centroid depths of 24 ± 2 km provided an adequate fit to the arrival times of these depth phases. Note that we could not include a slow layer corresponding to the sedimentary

cover for these models, so that this value is likely to be an overestimate. Including a sedimentary layer reduced depth estimates for other events by 1-3 km.

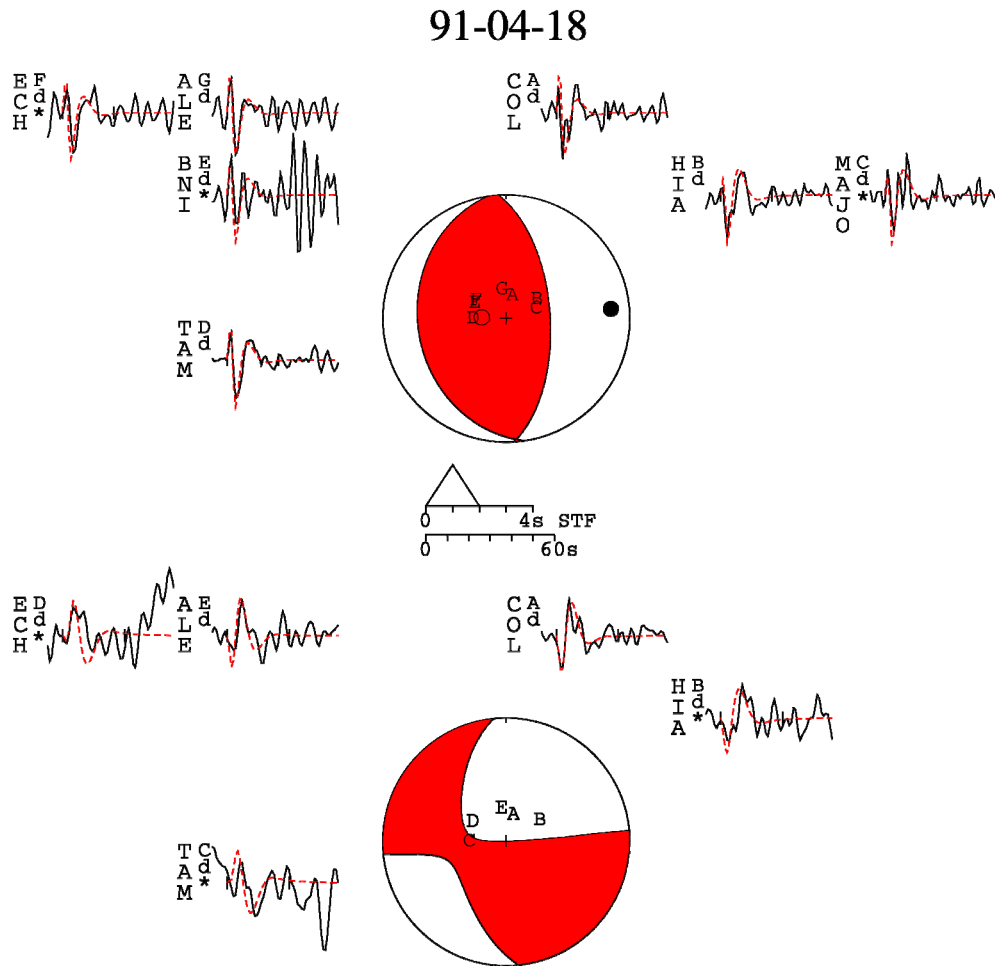
Sensitivity Tests

We performed sensitivity tests for each event that was inverted for all source parameters (i.e. the 1991-04-18, 1994-05-01, 2006-07-29a and 2006-07-29b events; Figures DR6-DR9). In each test, one parameter was fixed at a series of values either side of the best-fitting result, and all other parameters allowed to vary. Each value was varied until the entire parameter space was explored or the inversion no longer converged. Misfit between observed and calculated seismograms is given as the residual value divided by the data value (R/D, %; Figures DR6-DR9 A, C, E, G). Values of total model R/D (black lines in Figures DR6-DR9 A, C, E, G), *P*-wave R/D (blue lines) and *SH*-wave R/D (red lines) are shown. We also used MT5's *t* test function, based on the procedure outlined in Huang et al. (1986), to estimate formal error bounds (Figures DR6-9 B, D, F, H). This method tests whether misfit distributions for two given solutions differ significantly. For each parameter, we defined error bounds as the values at which the *t* statistic exceeded the acceptable value at the 95% confidence level (grey bars in Figures DR6-9 B, D, F, H).

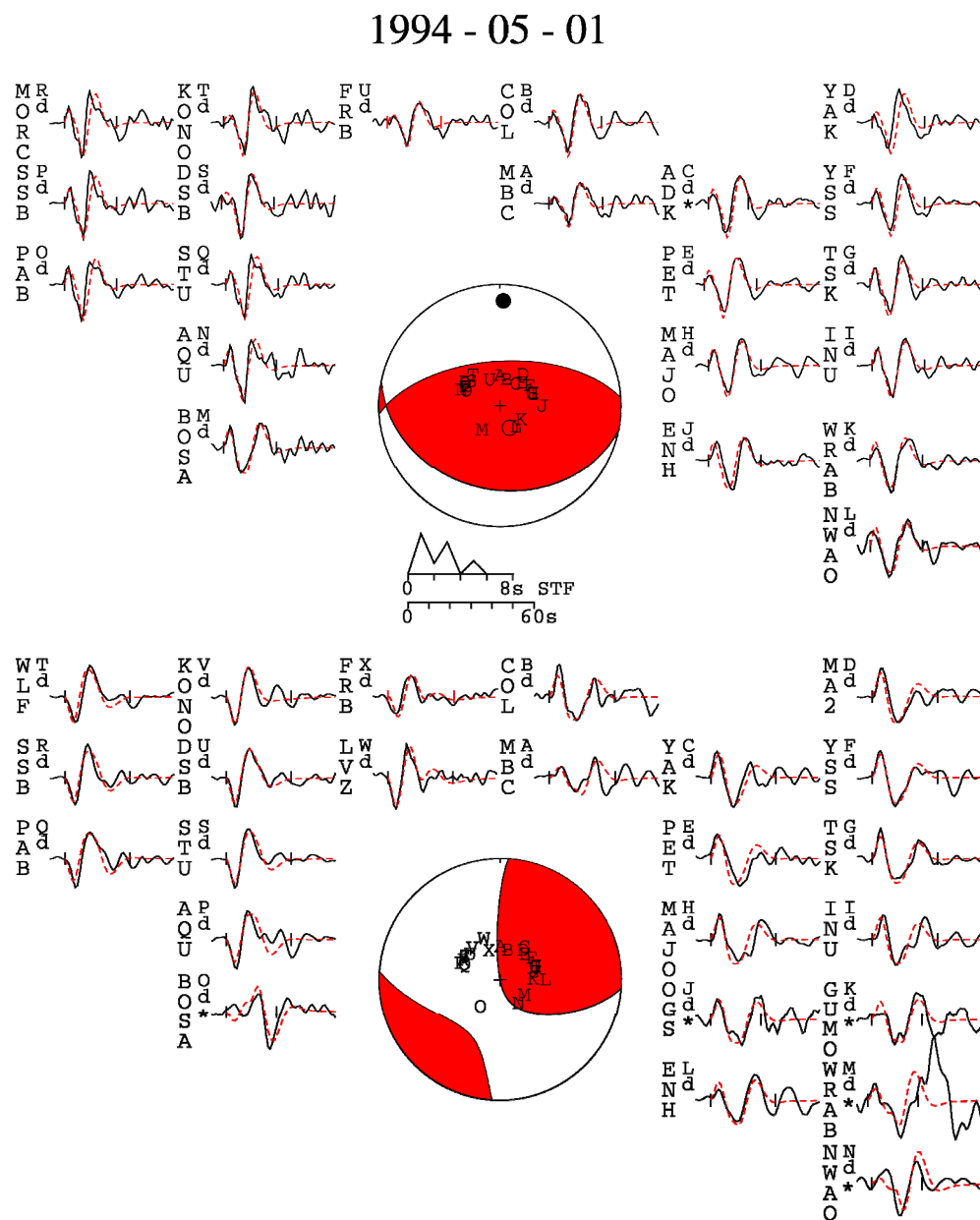
In general, parameter sweeps show clear R/D misfit minima at the best-fit solution. Both *P*- and *SH*-wave data were sensitive to depth, while *SH*-wave data were more sensitive than *P*-wave data to strike, dip and rake. This behavior is a result of each of the studied earthquakes being reverse faulting events and the majority of stations used plotting near the center of the focal sphere. As such, station coverage was poor around the *P*-wave nodal planes, but good around the *SH*-wave nodal planes.

T test results for depth sensitivity also generally show clear minima at the best-fit solution, with values indicating formal uncertainties of $\leq \pm 4$ km. These values are comparable to those reported by Huang et al. (1986) for events occurring along the Mid-Atlantic Ridge. This result implies that depth differences between E-W trending and N-S trending reverse faulting earthquakes that we discuss, close to 10 km, are resolvable by our methods. However, we stress that these formal error estimates are minima and that true estimates – considering uncertainties in, for example, the velocity model used – are likely to be larger, although difficult to quantify. *T* test results for strike, dip and rake sensitivity were less clean than those for depth and seemed to be strongly influenced by local minima in the misfit space, particularly for noisier events (i.e. 1991-04-18, 1994-05-01). The results are included for completeness but are likely only to be useful for general insight and are also subject to various uncertainties that are less easily quantified. Uncertainty estimates were $\leq \pm 35^\circ$ for strike, $\leq \pm 9^\circ$ for dip, $\leq \pm 38^\circ$ for rake. Again, these results imply that differences in strike and depth between the two populations of earthquakes we identify are resolved. These values are in broad agreement with the results of Abers et al. (1988), who applied similar techniques to several events at the nearby NW margin of the Hindu Kush.

81 Figure DR1. Results of teleseismic body wave-form inversion for the 18th April, 1991 event. *P*-
 82 wave seismograms are shown on the upper panel, *SH*-wave seismograms shown on the lower
 83 panel. Black solid lines = observed seismograms; red dashed lines = modeled seismograms; STF
 84 = source-time function; * = seismogram not included in inversion, forward model included as a
 85 visual check on result. Focal mechanisms are lower hemisphere projections of the focal sphere,
 86 where red areas = compressional quadrants; white areas = extensional quadrants; capital letters =
 87 seismogram tags, assigned according to azimuth, and plotted on the lower hemisphere projection
 88 at the point of intersection of the ray path. Seismogram scale bar is shown beneath the source
 89 time function. These conventions are used throughout Figures 2 – 4. Best-fitting centroid depth =
 90 3.7 km, $M_W = 5.4$.



93 Figure DR2. Results of teleseismic body wave-form inversion for the 1st May, 1994 event. Best-
94 fitting centroid depth = 20.8 km, $M_W = 6.0$.

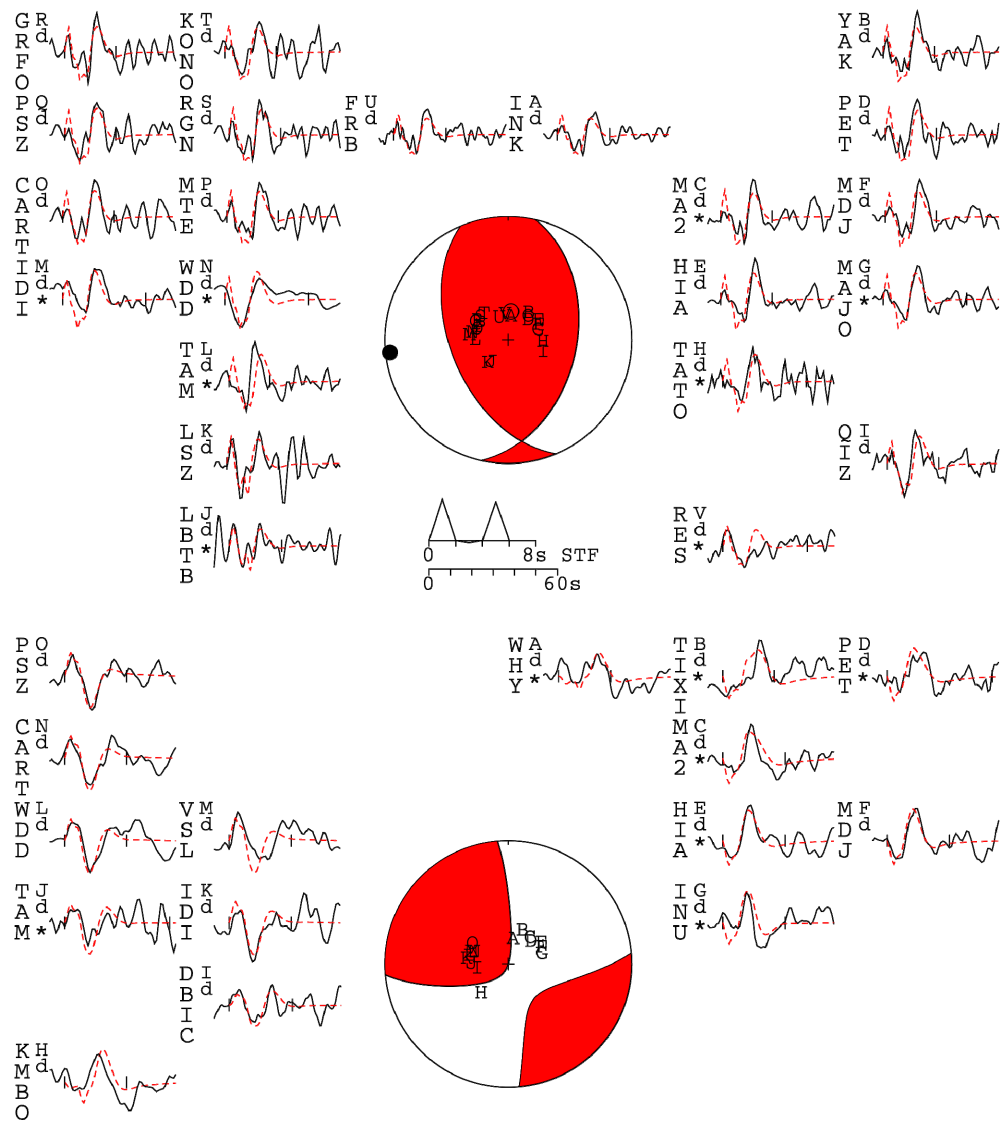


95
96

97 Figure DR3. Results of teleseismic body wave-form inversion for the first 29th July, 2006 event.

98 Best-fitting centroid depth = 11.6 km, $M_W = 5.3$.

06-07-29a

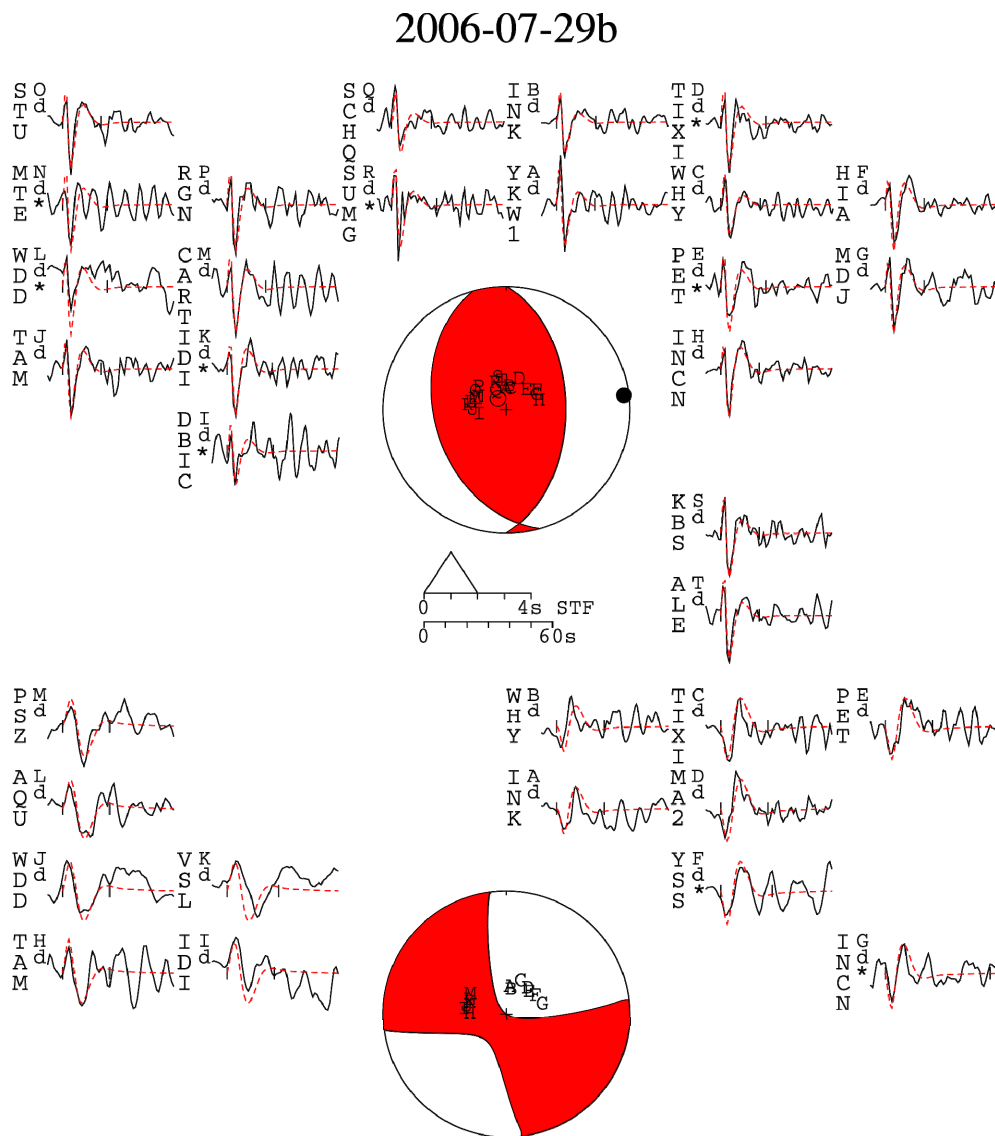


99

100

101 Figure DR4. Results of teleseismic body wave-form inversion for the first 29th July, 2006 event.

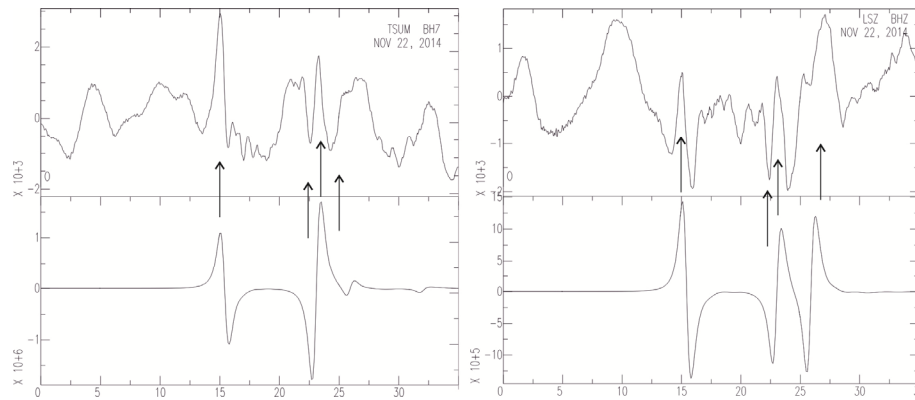
102 Best-fitting centroid depth = 3.9 km, $M_W = 5.4$.



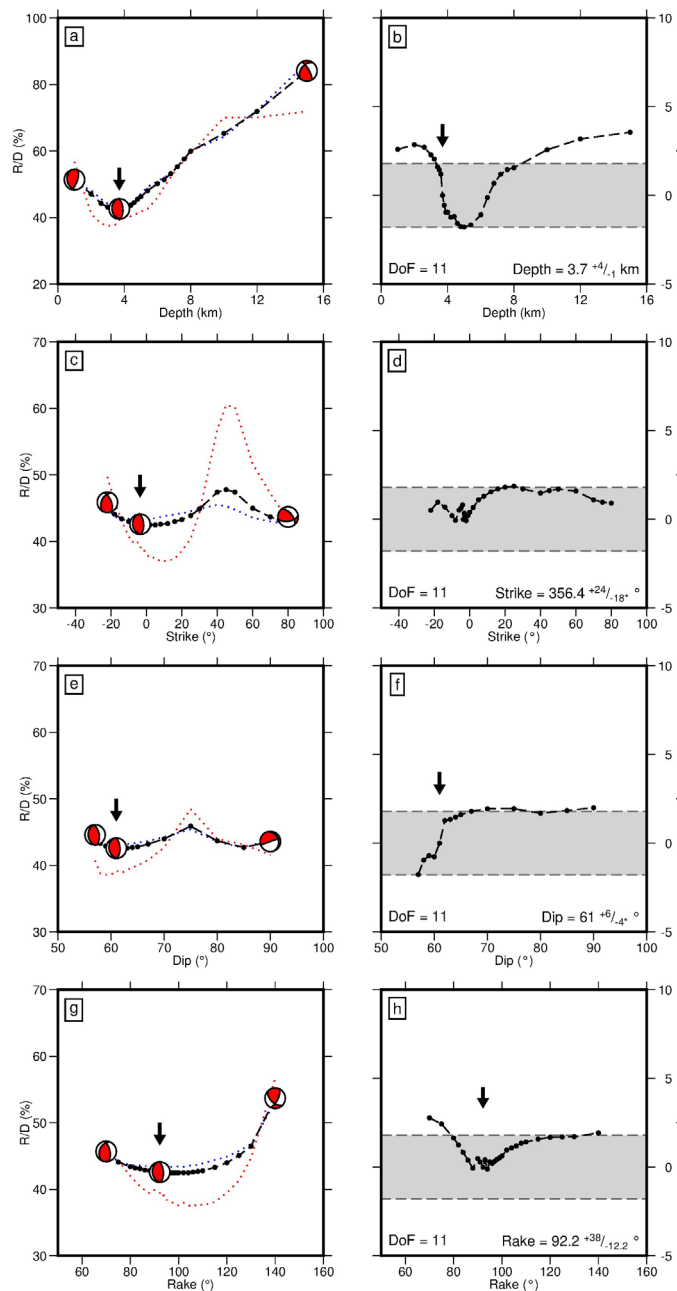
103

104

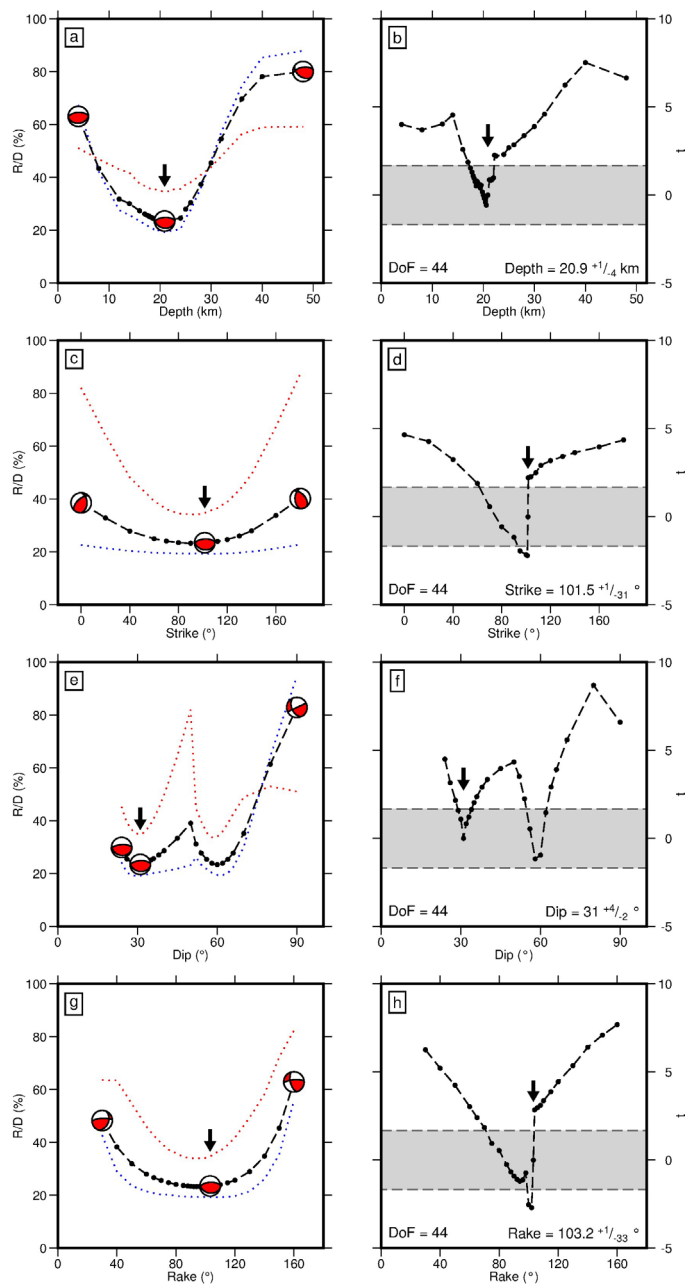
105 Figure DR5. Results of depth-phase modeling for the 24th November, 2014 event. Seismograms
106 from two stations (TSUM and LSZ) are shown as examples. Observed seismograms are shown
107 on the upper panels, while seismograms calculated assuming the CMT solution are shown on the
108 lower panels. Best-fitting centroid depth = 24 km.



111 Figure DR6. Sensitivity tests for the 18th April, 1991. Black arrows = best-fit solution. (A, C, E,
 112 G) Residual/Data misfit (R/D, %) as function of depth, strike, dip and rake. Black lines = total
 113 model R/D; blue lines = *P*-wave R/D; red lines = *SH*-wave R/D; focal mechanisms shown for
 114 selected models. (B, D, F, G) T-tests for depth, strike, dip and rake. Black lines = *t* value with
 115 respect to best-fit solution; grey bands = range of *t* values for which solutions have similar misfit
 116 distributions to best-fit solution at 95% confidence level; DoF = degrees of freedom.



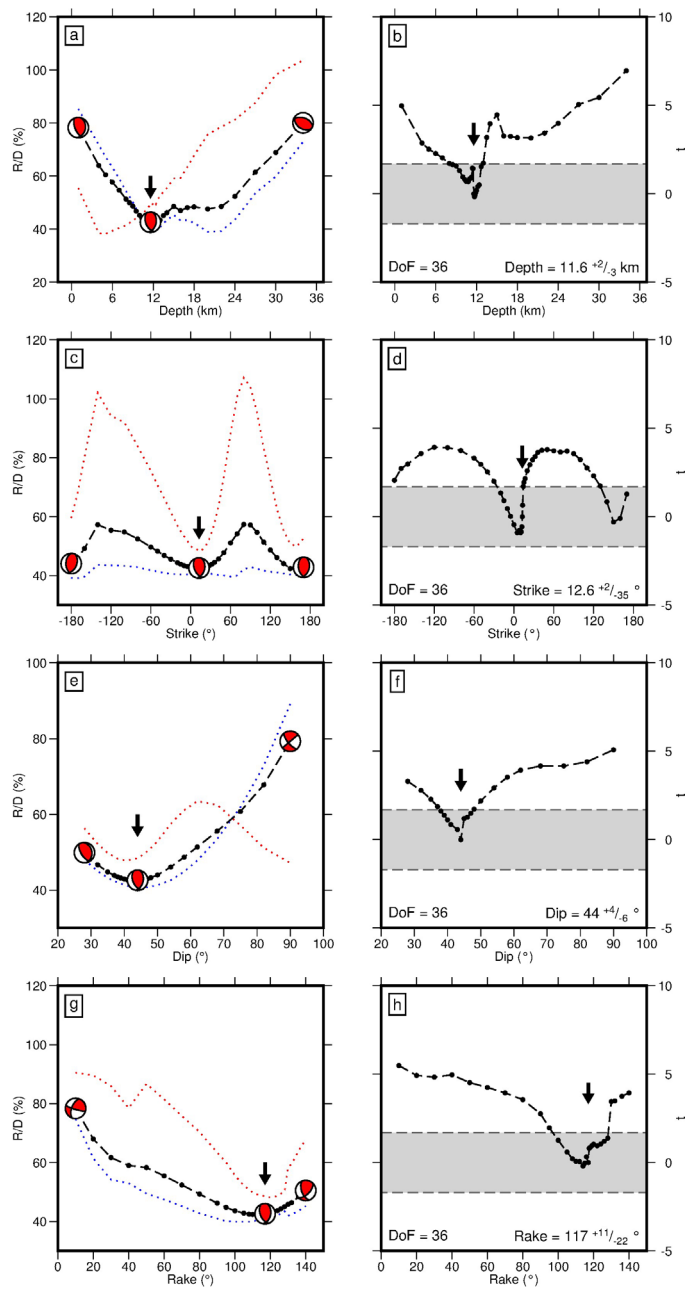
118 Figure DR7. As above, for the 1st May, 1994 event.



119

120

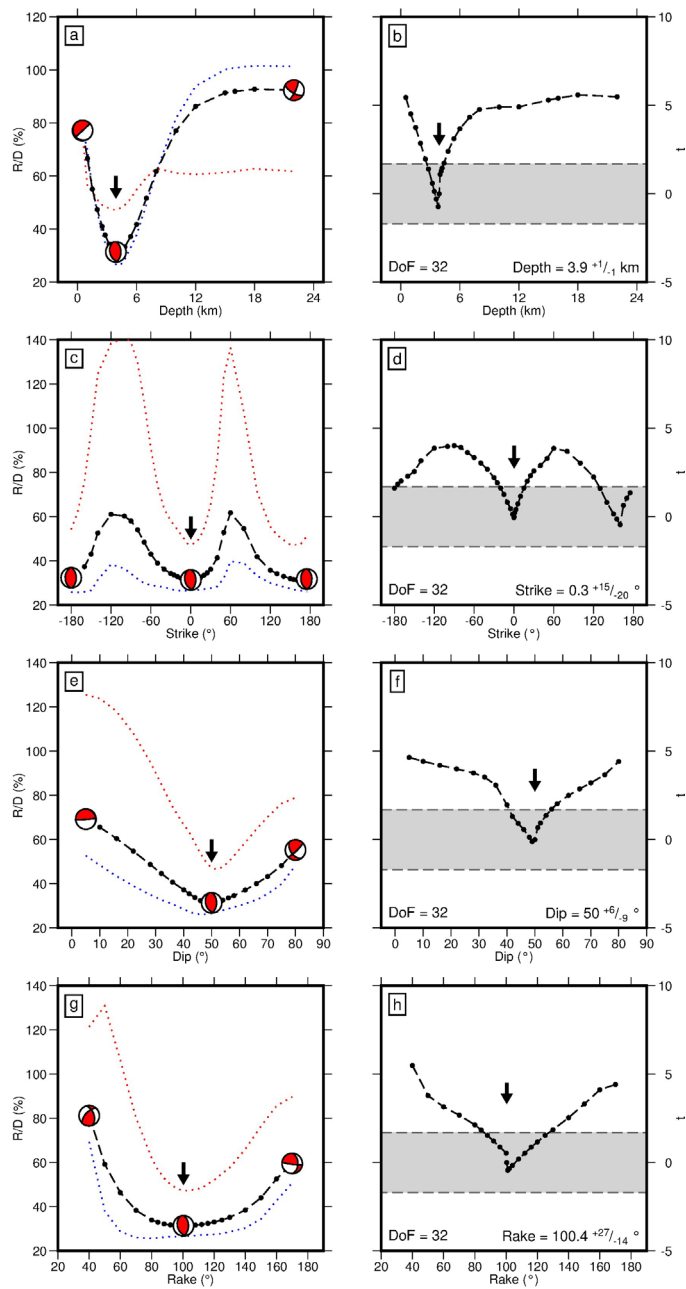
121 Figure DR8. As above, for the first 29th July, 2006 event.



122

123

124 Figure DR8. As above, for second 29th July, 2006 event.



125

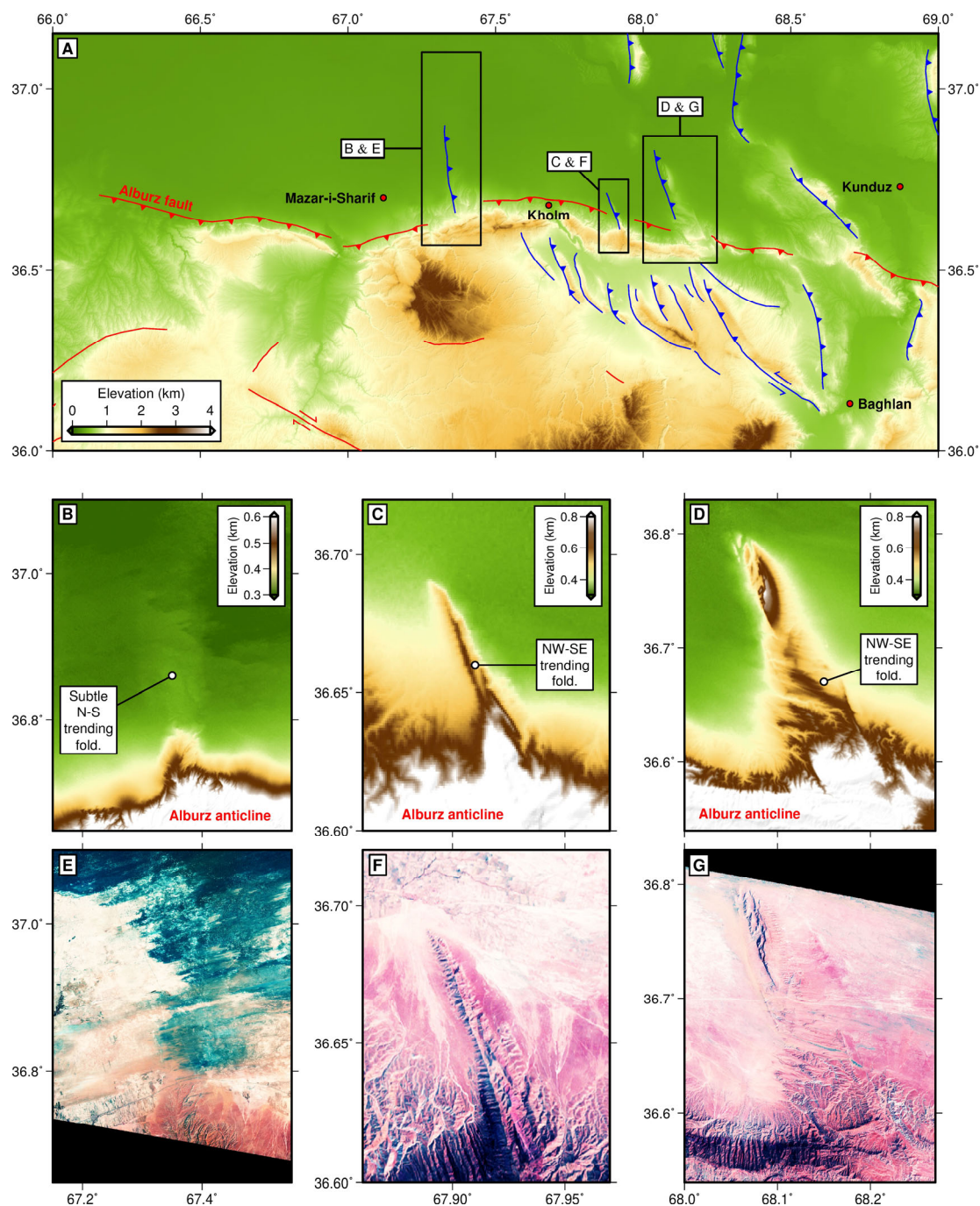
126

127 **GEOMORPHOLOGY**

128 In Figure DR10 we present additional topographic maps and Landsat images of
129 geomorphologic features at the southern margin of the Afghan-Tajik Depression. These images
130 highlight apparent cross-cutting relationships between the large, E-W trending Alburz fault and
131 smaller, approximately N-S trending anticlines.
132

Figure DR10. Geomorphologic features of the southern margin of the Afghan-Tajik Depression.

(A) Overview of the southern margin of the Afghan-Tajik Depression. Red lines = active faults related to N-S compression; blue lines = active faults related to E-W compression. (B, C, D) High resolution topographic images of the regions shown in (A). (E, F, G) RGB532 Landsat images of the regions shown in (A).



139 **REFERENCES CITED**

- 140 Abers, G., Bryan, C., Roecker, S. and McCaffrey, R., 1988, Thrusting of the Hindu Kush over
141 the southeastern Tadjik Basin, Afghanistan: evidence from two large earthquakes:
142 Tectonics, v. 7, no. 1, pp. 41-56, doi:10.1029/TC007i001p00041.
- 143 Brocher, T., 2005, Empirical relations between elastic wavespeeds and density in the Earth's
144 crust: Bulletin of the Seismological Society of America, v. 95, no. 6, pp. 2081-2092.
- 145 Bayasgalan, A., Jackson, J. and McKenzie, D., 2005, Lithosphere rheology and active tectonics
146 in Mongolia: relations between earthquake source parameters, gravity and GPS
147 measurements, Geophysical Journal International: v. 163, pp. 1151-1179,
148 doi:10.1111/j.1365-246X.2005.02764.x.
- 149 Chapman, C., 1978, A new method for computing synthetic seismograms: Geophysical Journal
150 of the Royal Astronomical Society, v. 54, no. 3, pp. 481-518.
- 151 Chapman, C., Yen-Yi, C. and Lyness, D., 1988, The WKBJ seismogram algorithm *in* Doornbos,
152 D.J. (ed.), Seismological Algorithms: Computational Methods and Computer Programs,
153 Academic: London, pp. 47-74.
- 154 Delouis, B., Déverchère, Melnikova, V., Radziminovitch, N., Loncke, L., Larroque, C., Ritz, J.F.
155 and San'kov, V., 2002, A reappraisal of the 1950 (Mw 6.9) Mondy earthquake, Siberia, and
156 its relationship to the strain pattern at the south-western end of the Baikal rift zone, Terra
157 Nova, v. 14, no. 6, pp. 491-500, doi:10.1046/j.1365-3121.2002.00445.x.
- 158 Emmerson, B., Jackson, J., McKenzie, D. and Priestley, K., 2006, Seismicity, structure and
159 rheology of the lithosphere in the Lake Baikal region: Geophysical Journal International, v.
160 167, pp. 1233-1272, doi:10.1111/j.1365-246X.2006.03075.x.

161 Huang, P. Y, Solomon, S. C., Bergman, E. A. and Nabelek, J. L., 1986, Focal depth mechanisms
 162 of Mid-Atlantic Ridge earthquakes from body waveform inversion: *Journal of Geophysical*
 163 *Research*, v. 91, no. B1, pp. 579-598.

164 Kennet, B., Engdahl, E. and Buland, R., 1995, Constraints on seismic velocities in the Earth from
 165 travel times, *Geophysical Journal International*: v. 122, pp. 108-124.

166 Kufner, S.-K., Schurr, B., Ratschbacher, L., Murodkulov, S., Abdulhameed, S., Ischuk, A.,
 167 Metzger, S. and Kakar, N., 2018, Seismotectonics of the Tajik basin and surrounding
 168 mountain ranges: *Tectonics*, v. 37, doi:10.1029/2017TC004812.

169 McCaffrey, R. and Abers, G., 1998, SYN3: a program for the inversion of teleseismic body
 170 waveforms on microcomputers: Air Force Geophysics Laboratory Technical Report AFGL-
 171 TR-0099.

172 McCaffrey, R., Zwick, P. and Abers, G., 1991, SYN4 program: IASPEI Software Library, v. 3.

173 Sloan, R.A, Jackson, J.A., McKenzie, D. and Priestley, K., Earthquake depth distributions in
 174 central Asia, and their relations with lithosphere thickness, shortening and extension:
 175 *Geophysical Journal International*, v. 185, pp. 1-29, doi:10.1111/j.1365-246X.2010.04882.x.

176 Zwick, P., McCaffrey, R. and Abers, G., 1994, MT5 Program: IASPEI Software Library, v. 4.